

# AGN-driven outflow shuts down star formation in a $z = 4$ recently quenched galaxy

PO-FENG WU<sup>1</sup>

<sup>1</sup>*Institute of Astrophysics, National Taiwan University, Taipei 10617, Taiwan*

## ABSTRACT

The confirmation of massive quiescent galaxies emerging within the first billion years of the universe poses intriguing questions about the mechanisms of galaxy formation. There must be highly efficient process at work to shut down star formation in galaxies at cosmic dawn. I present the detection of neutral outflowing gas in a massive ( $M_* = 1.2 \times 10^{11} M_\odot$ ) recently quenched AGN-host galaxy at  $z = 4$  as a evidence that AGN-driven outflows could be one such mechanism. Based on JWST spectrum, the star formation rate of this has been declining with a rapid e-folding timescale of  $\sim 50$  Myrs. The current specific star formation rate is  $5 \times 10^{-11} \text{ yr}^{-1}$ , roughly 40 times lower than that of the star-forming main sequence at comparable redshifts. Emission line ratios of [Ne III]/[O II] and [O III]/H $\beta$  emission indicate the presence of an AGN. A series of Fe II and Mg II absorption lines appear blueshifted by  $\sim 250 \text{ km s}^{-1}$  relative to the stellar continuum, suggesting an outflow of neutral gas. The estimate mass outflow rate is approximately 7 times greater than star formation rate derived from the stellar continuum, implying that the suppression of star formation is likely due to gas being depleted by the AGN-driven outflow. This galaxy represents the most distant example of its kind known to date. This study offers a compelling explanation for the existence of massive quiescent galaxies in the first billion years of the universe.

## 1. INTRODUCTION

Large extra-galactic imaging surveys have revealed that the rest-frame optical colors of galaxies exhibit a bimodal distribution (Strateva et al. 2001; Baldry et al. 2004; Bell et al. 2004; Willmer et al. 2006; Franzetti et al. 2007). Galaxies with blue colors are typically those with active in-situ star formation, whereas red galaxies show minimal star formation activities. Based on redshifts and restframe colors derived from broadband and medium band spectral energy distribution (SED) fitting, a population of massive (several  $10^{10} M_\odot$ ) red galaxies has been identified in the first two billion years of universe (Ilbert et al. 2013; Muzzin et al. 2013; Straatman et al. 2014). In addition to their rapid formation, what makes these galaxies even more intriguing is their early quiescence. Despite the overall increase in cosmic star formation rate density during this period (Madau & Dickinson 2014), there must have been highly efficient mechanisms in the early universe that truncated star formation activities in these galaxies.

However, photometric SED fitting can introduce significant uncertainties in redshifts and restframe colors. Spectroscopic follow-up observations have demonstrated that many galaxies initially identified as massive with  $z_{\text{phot}} > 3$  are in fact lower-redshift dusty star-forming galaxies (Forrest et al. 2024). Nevertheless, deep near-

IR spectroscopic observations have confirmed the existence of dozens of massive quiescent galaxies at  $z > 3$  (Marsan et al. 2015; Schreiber et al. 2018; Forrest et al. 2020a; D'Eugenio et al. 2021; Forrest et al. 2022; McConachie et al. 2022; Tanaka et al. 2024; Setton et al. 2024), highlighting a population that current numerical simulations struggle to reproduce, especially the most massive ones (Forrest et al. 2020b).

Furthermore, several massive quiescent galaxies at  $z > 4$  have also been spectroscopically confirmed, both through their faint emission lines and stellar populations, as constrained by stellar continuum absorption (Tanaka et al. 2019; Carnall et al. 2023; Kakimoto et al. 2024; de Graaff et al. 2024; Frye et al. 2024; Carnall et al. 2024). Full-spectral fitting of the stellar continua indicates that most of these galaxies build up the bulk of their stellar masses during a brief but intense period of star formation. During this phase, the star-formation rate (SFR) peaks at least a few hundred  $M_\odot \text{ yr}^{-1}$ , followed by a rapid truncation with an exponential decaying timescale on the order of  $\sim 100$  Myr. This violent process is not a typical mode of star formation at  $z \sim 4$ , where the gas depletion time through star formation,  $M_{\text{gas}}/\text{SFR}$ , is generally several hundred Myrs for most star-forming galaxies (Dessauges-Zavadsky et al. 2020). Therefore, the abrupt decline in SFR in these qui-

escent galaxies must have been triggered by additional processes.

Theoretically, active galactic nuclei (AGNs) are believed to be pivotal in halting star formation and maintaining the quiescence of galaxies. The mass accretion onto the central supermassive black hole (SMBH) can release vast amounts of energy, heating the gas and inducing turbulence, thereby suppressing star formation. Even more critically, AGN can drive powerful outflows, expelling gas from the galaxy and rapidly depleting the gas reservoir on much shorter timescales (Di Matteo et al. 2005).

While theoretically compelling, direct evidence linking AGN-driven outflows to the quenching of star formation remains elusive. If AGN-driven outflows are indeed instrumental in this process, one would expect to find signs of such activities in quiescent galaxies that have recently experienced a decline in their star-formation rates (SFRs). These recently quenched galaxies, often referred to as post-starburst galaxies, are valuable sources for studying quenching mechanisms at lower redshifts. At  $z < 1.5$ , a few studies have reported high-velocity outflows of neutral gas, reaching speeds of  $\sim 1000 \text{ km s}^{-1}$  in post-starburst galaxies. However, these galaxies do not show clear signs of AGN activity (Tremonti et al. 2007; Maltby et al. 2019).

James Webb Space Telescope (JWST) has recently enabled the measurement of interstellar medium (ISM) absorption in massive quiescent galaxies at higher redshifts, thanks to its extended wavelength coverage and enhanced sensitivities. D'Eugenio et al. (2023) and Belli et al. (2024) reported the discovery of two young quiescent AGN-host galaxies at  $z \simeq 2.5$  and  $z \simeq 3$ , where the neutral outflow rate surpasses their SFRs by an order of magnitude. These outflows are depleting gas reservoirs more rapidly than star formation. These findings are claimed to be a smoking gun for feedback from SMBHs, potentially explain the presence of massive quiescent galaxies at higher redshifts.

In this paper, I extend the redshift frontier, presenting new evidence for AGN-driven outflows as a quenching mechanism at  $z \simeq 4$ . I will discuss the detection of neutral gas outflow and the corresponding outflow rate traced by Mg II and Fe II absorption lines in a massive, recently quenched AGN-host galaxy at  $z = 4.1$ . This galaxy currently represents the highest-redshift example of its kind known to date.

In Section 2, I introduce the target galaxy and observations conducted. Section 3 describes the modeling of restframe optical spectra for the star-formation history (SFH) and ionized line emissions. In Section 4, I calculate the physical properties of the neutral gas out-

flow. The implications of these findings are discussed in Section 5, and the key takeaways are summarized in Section 6.

## 2. THE TARGET

The galaxy discussed in this paper was first reported by Frye et al. (2024) as a quiescent galaxy with spectroscopic redshift  $z = 4.1076 \pm 0.0023$ . This observation was conducted as part of the JWST Director's Discretionary Time (DDT) program (PID: 4446, PI: B. Frye). The spectra were obtained using the NIRSpec Micro-Shutter Array (MSA) with the grating/filter combinations G140M/F100LP and G235M/F170LP, providing a spectral resolution  $R \sim 1000$ . The on-source exposure times are 4420 seconds for G140M/F100LP and 6996 seconds for G235M/F170LP. For further details on the observation setting, readers are referred to Frye et al. (2024).

Figure 1a shows the galaxy image in NIRCам/F200W from the same JWST program. I use *galfit* (Peng et al. 2010) to fit a single Sérsic profile to the 2D light distribution. The point-spread function (PSF) is determined by stacking images of bright stars. According to the best-fit model, the galaxy has an AB magnitude of  $m_{AB, F200W} = 23.1$ , an effective radius  $R_e = 390 \text{ pc}$ , a Sérsic index  $n = 5.3$ , and an axis ratio of 0.6. This analysis reveals that the galaxy is a compact, flattened spheroid.

Comparing the flux of the spectrum at the same wavelength (Figure 1b), I estimate a slit loss of 50%. From the slit spectrum, I derive a stellar mass of  $M_* = 6 \times 10^{10} M_\odot$  (see Section 3). Assuming the mass-to-light ratio is the same inside and outside the slit, the total mass of this galaxy is  $M_* = 1.2 \times 10^{11} M_\odot$ . The effective radius of this galaxy is broadly consistent with other quiescent galaxies ( $< 1 \text{ kpc}$ , Tanaka et al. 2019; Carnall et al. 2023; de Graaff et al. 2024) and is several times smaller than that of star-forming galaxies with similar stellar masses and redshifts (Ward et al. 2024).

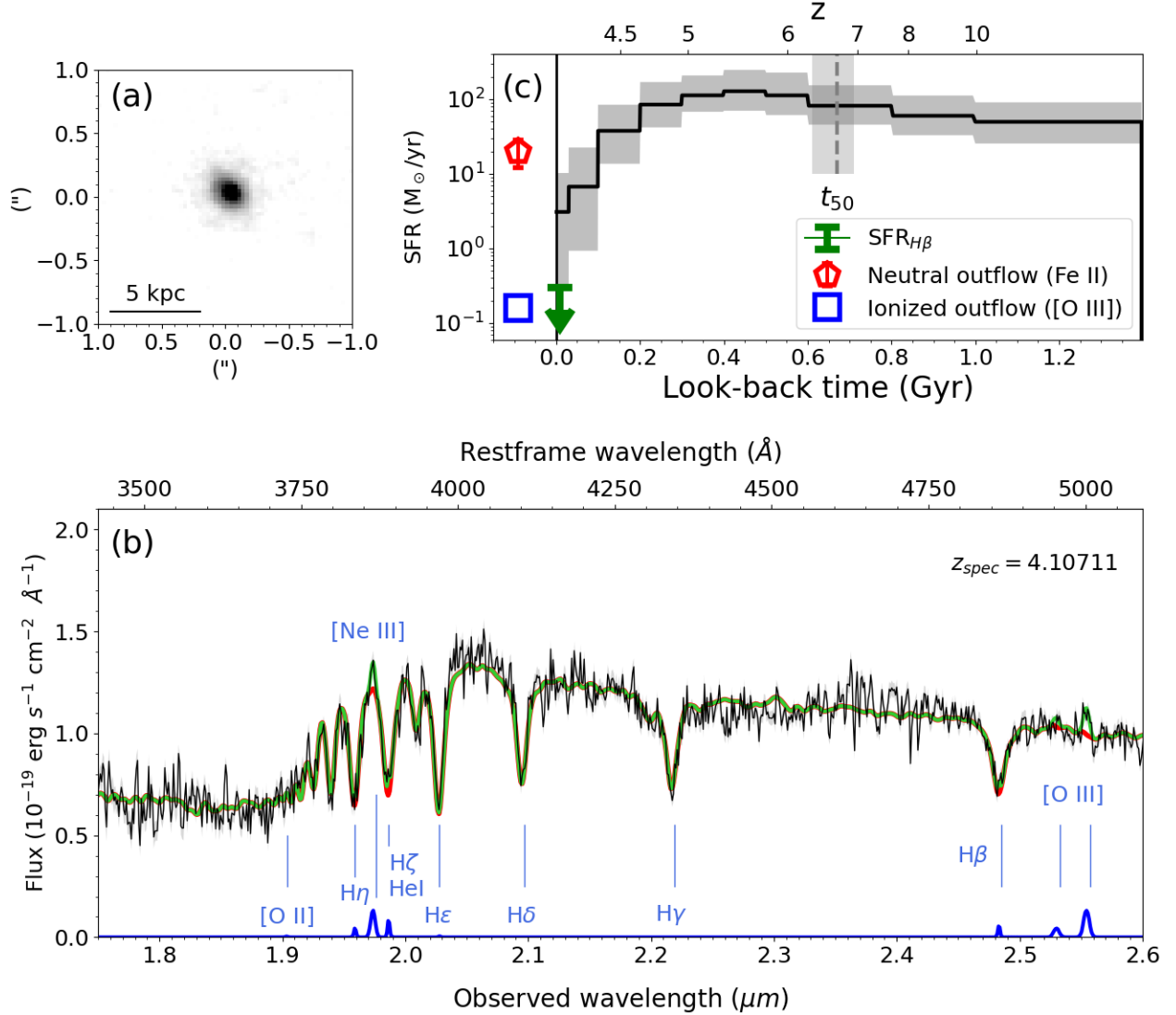


**Figure 1.** (a) The  $2'' \times 2''$  F200W cutout image of the galaxy. (b) The restframe optical spectrum of the galaxy (black) and the best-fit models. The blue line represents the emission line component derived from the pPXF fit, while the red line shows the stellar continuum model from BAGPIPES. The green line denotes the sum of the red and the blue components. The spectrum indicates a low sSFR as no prominent star formation indicators, such as [O II] and H $\beta$ , are detected with high significance. The weak but yet reliable detections of [Ne III] and [O III] suggest the presence of an AGN (see Figure 2). (c) The SFH of the galaxy, as constrained by the stellar continuum. The black line and the shaded region represent the median and the 16th and 84th percentiles of the posterior distributions, respectively. The galaxy formed half of its stellar mass at  $z \sim 6.7$ , indicated by the vertical dashed line. The SFR peaked at a lookback time of  $\sim 400 \text{ Myr}$  and declined from  $\sim 130 M_{\odot} \text{ yr}^{-1}$  to  $\sim 3 M_{\odot} \text{ yr}^{-1}$ . The upper limit of the SFR derived from the H $\beta$  emission line flux (green arrow) is also well below the star-formation main sequence (Section 3). The red pentagon and blue square represent the outflow rates of neutral and ionized gas, respectively (Section 4). The error bar for the neutral outflow reflects uncertainty from the column density, while the error for the ionized outflow, constrained by flux measurements, is smaller than the label. Systematic uncertainties are not included in the error bar (see Section 4). The quantities are all measured from flux in the slit and not corrected for the 50% slit loss.

### 3. STELLAR POPULATION AND IONIZED GAS

The G235M grism spectrum covers the restframe optical wavelengths, encompassing age-sensitive stellar absorption lines and prominent ISM emission lines (Figure 1b). I use the spectrum between 3480 Å and 5200 Å in the restframe to constrain the stellar population and the star formation history (SFH) of the galaxy. Unless stated otherwise, the quantities reported are based on the fluxes measured through the slit, with no correction applied for the 50% slit loss.

#### 3.1. Modeling the emission lines

A close visual inspection of the spectrum reveals weak emission lines of [Ne III]λ3869 and [O III]λ5007 but no prominent Balmer emission and [O II]λ3727, 3729 doublet. To determine the fluxes and velocities of these emission lines, I use the Penalized Pixel-Fitting method (pPXF, Cappellari & Emsellem 2004; Cappellari 2017, 2023), which fits a model comprising both the stellar continuum and gas emission. The stellar template is based on the UV-extended E-MILES stellar population synthesis models (Vazdekis et al. 2016). All emission lines are modeled as a single kinematic component. Each line is described as a Gaussian and all lines have the same velocity and velocity dispersion. The strength of each line is treated as a free parameter, with the exception of [O III], where the flux ratio of [O III]λ5007/[O III]λ4959 is fixed at 3.

The emission line model will be subtracted from the spectrum prior to fitting the SFH. The best-fit emission line model is shown as the blue curve in Figure 1b, and Table 1 lists the fluxes of relevant emission lines. As observed visually, the only two emission lines with significant detection are [Ne III]λ3869 ( $S/N \simeq 7$ ) and [O III]λ5007 ( $S/N \simeq 8$ ). These emission lines are slightly blueshifted relative to the stellar continuum, with a velocity of 324 km s<sup>-1</sup>. The [O II]λ3727,3729 doublet, which is typically prominent and often observed in quiescent galaxies (Maseda et al. 2021), is not

**Table 1.** Emission line properties

Line	flux (10 <sup>-19</sup> ergs cm <sup>-2</sup> s <sup>-1</sup> )
[O II]λ3727, 3729	0.28 ± 0.29
N III] λ3869	1.44 ± 0.20
Hζ, He I λ3889	0.23 ± 0.10
Hβ	0.23 ± 0.11
O III]λ5007	2.08 ± 0.25

<sup>a</sup> Line velocity  $v = -324$  km s<sup>-1</sup>. Line velocity dispersion  $\sigma = 279$  km s<sup>-1</sup>

detected either in the fitting or visually. Hβ is only marginally detected at  $\sim 2\sigma$  significance.

Figure 2 presents a comparison of the line ratios of the target quiescent galaxy with those of emission-line galaxies from various studies across a broad redshift range: SDSS DR7 at  $0.08 < z < 0.12$  (Abazajian et al. 2009), the CLEAR survey at  $1.1 < z < 2.5$  (Simons et al. 2023), the CEERS survey at  $z > 1.7$  (Backhaus et al. 2024), and the stack spectra from galaxies in different stellar mass bins from the MOSDEF survey at  $z \sim 2.3$  and  $z \sim 3.3$  (Sanders et al. 2021). Only galaxies with  $S/N > 2$  for all 4 lines are plotted. The dashed line in Figure 2 delineates the boundary between AGN and H II regions, as proposed by Backhaus et al. (2022).

For the quiescent galaxy, the lower limit of [Ne III]/[O II], calculated using a  $2\sigma$  limit for [O II], exceeds all other galaxies shown in the comparison. Combined with the [O III]/Hβ of approximately 10, these line ratios strongly suggest that the source of ionizing photons is likely AGN rather than H II regions. Additionally, the pPXF fitting indicate a marginal detection ( $S/N \sim 2$ ) of Hζ or He I emission at 3889 Å. Given the weak Hβ, the emission is unlikely Hζ. The presence of He I emission and the high line ratios can be attributed to a weak AGN.

#### 3.2. Modeling the star formation history

I use the code BAGPIPES (Carnall et al. 2018) to fit the spectrum and constrain the SFH. The stellar continuum templates are generated with the 2016 revised version of the Bruzual & Charlot (2003) population synthesis model (Chevallard & Charlot 2016) using the E-MILES stellar spectral library (Falcón-Barroso et al. 2011; Vazdekis et al. 2016). The models are convolved with a Gaussian kernel in velocity space to account for the stellar velocity dispersion of the galaxy.

The dust attenuation law follows the model of Salim et al. (2018), which is parameterized as a power-law deviation from the Calzetti dust law (Calzetti et al. 2000). The Salim et al. (2018) dust law also incorporates a Drude profile to model the 2175 Å bump, though this feature is irrelevant here. For stars younger than 10 Myrs, a different attenuation is permitted and is parameterized as  $\eta$ , the ratio of attenuation in magnitudes between the young and the old populations.

Based on the redshift reported by Frye et al. (2024), I allow the redshift to vary within a narrow range  $4.09 < z < 4.12$ . I adopt a non-parametric SFH with 11 age bins, defined by bin edges at 0, 10, 30, 100, 200, 300, 400, 500, 600, 800, 1000 Myrs, and the age of the universe. In this model, the SFR within each age bin is assumed to be constant. The model fits for  $\Delta \log(SFR)$

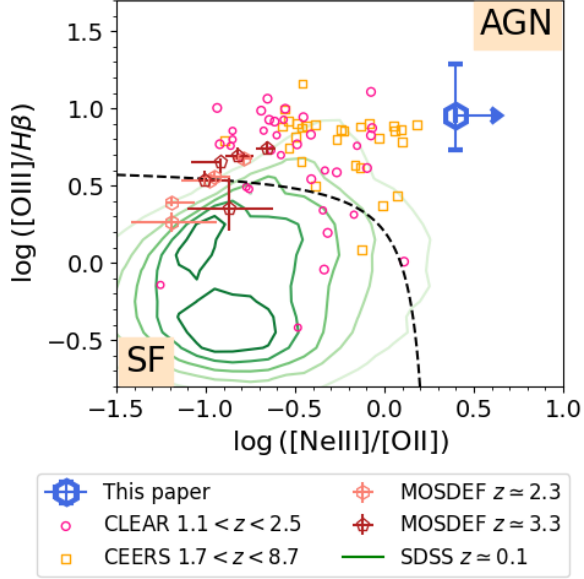


**Figure 2.** The  $[\text{Ne III}]/[\text{O II}]$  v.s.  $[\text{O III}]/\text{H}\beta$  line ratio of the galaxy (blue hexagon). I use the  $2\text{-}\sigma$  upper limit for  $[\text{O II}]$  to calculate the lower bound of  $[\text{Ne III}]/[\text{O II}]$ . For comparison, several samples of emission-line galaxies from various projects are plotted: SDSS at  $z \simeq 0.1$  (green contours, Abazajian et al. 2009), CLEAR at  $1.1 < z < 2.5$  (magenta circles, Simons et al. 2023), CEERS at  $z > 2$  (yellow squares, Backhaus et al. 2024), and stacked spectra of MOSDEF at  $z \sim 2.3$  and  $z \simeq 3.3$  (round and orange pentagons, Sanders et al. 2021). The black dashed line represents the boundary between star formation and AGN ionization (Backhaus et al. 2022). The quiescent galaxy exhibits the highest  $[\text{Ne III}]/[\text{O II}]$  and  $[\text{O III}]/\text{H}\beta$  line ratios among galaxies measured, suggesting it likely hosts an AGN.

between adjacent time bins, with the Student’s-t distribution used for the prior, following the approach in Leja et al. (2019). I have tested various age bin configurations and found that the main conclusions of this paper are robust as long as sufficient time resolution is provided for the last few hundred Myrs. Additionally, I use a double power-law parametric form:  $\psi(t) \propto [(t/\tau)^\alpha + (t/\tau)^{-\beta}]^{-1}$ , to derive the SFH, and the main conclusions remain consistent.

To address the potential issue with spectrophotometric calibration, I incorporate a second-order Chebyshev polynomial perturbation and a white noise model into the spectroscopic data. This approach accounts for possible mismatch in the overall shape between the spectrum and the models, as well as any potential underestimation of the uncertainties.

The emission-line model (Section 3.1) is subtracted from the observed spectrum, leaving only the stellar continuum is for model constraints. BAGPIPES employs a Bayesian approach to determine the most probable pa-

rameters. Table 2 presents the priors and posteriors for the model parameters.

Figure 1c illustrates the SFH of the quiescent galaxy. The galaxy formed half of its stellar mass  $\sim 670$  Myr ago, corresponding to  $z \sim 6.7$ . The SFR peaked around 400 Myr ago, then decreased sharply from  $\sim 130 M_\odot \text{ yr}^{-1}$  to the current rate of  $3 M_\odot \text{ yr}^{-1}$  – a 40-fold decline, equivalent to an e-folding timescale of  $\sim 50$  Myrs in the past 200 Myrs. The present specific SFR (sSFR) is  $5 \times 10^{-11} \text{ yr}^{-1}$ , roughly 40 times lower than the star-forming main sequence at  $z = 4$  (Popesso et al. 2023).

I also calculate the current SFR using the flux of  $\text{H}\beta$  emission. After correcting for the dust attenuation as constrained by the stellar continuum (Table 2), including attenuation from birth clouds, the derived  $\text{SFR}_{\text{H}\beta}$  is  $0.3 M_\odot \text{ yr}^{-1}$ , which is even lower than the SFR constrained by the stellar continuum. Moreover, this value should be considered an upper limit, as the  $\text{H}\beta$  emission is likely dominated by the AGN.



**Table 2.** Priors and posteriors for the SFH fitting

Component	Parameter	Symbol / Unit	range	Prior	Hyperparameters	Posterior
SFH	Redshift	$z$	(4.09, 4.12)	uniform		$4.10711^{+0.00026}_{-0.00023}$
	Stellar velocity dispersion	$\sigma/\text{km/s}$	(30, 500)	logarithmic		$330^{+17}_{-18}$
	Stellar mass formed	$M_*/M_\odot$	( $10^{10}$ , $10^{12}$ )	logarithmic		$10.80^{+0.21}_{-0.14}$
	Stellar metallicity	$Z/Z_\odot$	(0.01, 2)	logarithmic		$0.46^{+0.22}_{-0.14}$
Dust	Dust attenuation at 5500Å	$A_v$ / mag	(0, 5)	uniform		$0.44^{+0.45}_{-0.28}$
	Deviation from Calzetti slope	$\delta$	(-0.3, 0.3)	Gaussian	$\mu = 0$ $\sigma = 0.1$	$0.009^{+0.086}_{-0.077}$
	Birth cloud attenuation ratio	$\eta$	(1, 4)	uniform		$2.68^{+0.79}_{-0.98}$
Calibration	0th order		(0.75, 1.25)	Guassian	$\mu = 1$ $\sigma = 0.25$	$1.04^{+0.12}_{-0.15}$
	1st order		(-0.5, 0.5)	Guassian	$\mu = 0$ $\sigma = 0.25$	$0.12^{+0.09}_{-0.06}$
	2nd order		(-0.5, 0.5)	Guassian	$\mu = 0$ $\sigma = 0.25$	$-0.04^{+0.01}_{-0.01}$
Noise model	White noise scaling		(1, 10)	logarithmic		$1.92^{+0.04}_{-0.05}$

#### 4. DIAGNOSTICS OF GAS FLOW

The G140M grism spectrum provides coverage for various tracers for neutral gas in the restframe UV wavelength range. I use the ISM absorption spectrum, along with emission lines in the restframe optical (Section 3.1), to quantify the physical properties of neutral and ionized gas in this quiescent galaxy. The same as in Section 3, the quantities are reported without the slit loss applied.

##### 4.1. Modeling the ISM absorption

The top panel of Figure 3 shows the restframe UV spectrum. Within this wavelength range, the most prominent absorption feature is the Mg II  $\lambda 2796, 2803$  doublet. Additionally, several Fe II lines are clearly visible, including  $\lambda 2344$ , 2383, 2586, and 2600. There is also a hint of the weaker Fe II  $\lambda 2374$  line, although the absorption is consistent with the uncertainties.

These UV absorptions may originate from both gas in the foreground and the atmosphere of A-type and later spectral type stars. The red line in Figure 3 represents the rescaled model of the stellar continuum, derived from the stellar population constraints obtained from the restframe optical spectrum (Section 3.2). The rescaling involves comparing the median flux within  $\pm 100\text{\AA}$  of the observed and model spectra at each wavelength. The middle row of Figure 3 illustrates that the observed strengths of the observed Mg II and Fe II absorption lines exceed what can be explained by the stellar continuum alone. Therefore, the additional absorption is attribute to the foreground gas.

The bottom row of Figure 3 shows the absorption attributed to the gas. The observed and model spectra are resampled onto a common  $0.3\text{\AA}$  grid in the restframe. The observed spectrum is then divided by the model continuum, resulting the black line shown. This

division normalizes the spectrum to the stellar continuum. Visual inspection suggests that the gas absorption features are blueshifted by  $\sim 200\text{ km s}^{-1}$  relative to the stellar continuum.

To model the gas absorption, I use the formulation from Rupke et al. (2005), for the relative intensity as a function of wavelength, given by:  $I(\lambda) = 1 - C_f + C_f e^{-\tau(\lambda)}$ , where  $C_f$  is the gas covering fraction. When  $\tau(\lambda) = 0$ ,  $I(\lambda) = 1$ . As  $\tau(\lambda)$  increases,  $I(\lambda)$  approaches  $1 - C_f$  when  $\tau(\lambda) \rightarrow \infty$ . Given that the fluxes at the bottom of the Mg II  $\lambda 2796, 2803$  and Fe II  $\lambda 2383, 2586, 2600$  absorption lines are close to zero, it indicates that  $C_f$  must be close to 1.

The optical depth  $\tau(\lambda)$  is modeled as a Gaussian:  $\tau(\lambda) = \tau_0 e^{-(\lambda - \lambda_0)^2 / (\lambda_0 b_D / c)^2}$ , where  $\tau_0$  is the optical depth at the line center,  $\lambda_0$  is the central wavelength of the line,  $b_D$  is the Doppler parameter, which relates to the velocity width of the absorption, and  $c$  is the speed of light. While the covering fraction could in principle be a function of wavelength (Martin & Bouché 2009), it is assumed to be a constant here due to the lower spectral resolution. For a doublet, the combined intensity is given by  $I(\lambda) = 1 - C_f + C_f e^{-\tau_1(\lambda) - \tau_2(\lambda)}$ , where  $\tau_1(\lambda)$  and  $\tau_2(\lambda)$  are the optical depths for the two lines of the doublet.

The five Fe II lines ( $\lambda 2344, 2374, 2383, 2586, 2600$ ) are modeled together as one single Doppler component. The ratios among  $\tau_0$  of each Fe II transition are fixed based on their oscillation strength (Morton 2003). Similarly, the two Mg II lines are modeled as one single Doppler component, and the ratio between the  $\tau_0$  is fixed. A Gaussian noise is added to the model for 1,000 iterations to simulate the formal error spectrum and determine uncertainties of the model parameters (Table 3). Both the Fe II and Mg II absorptions are found to be

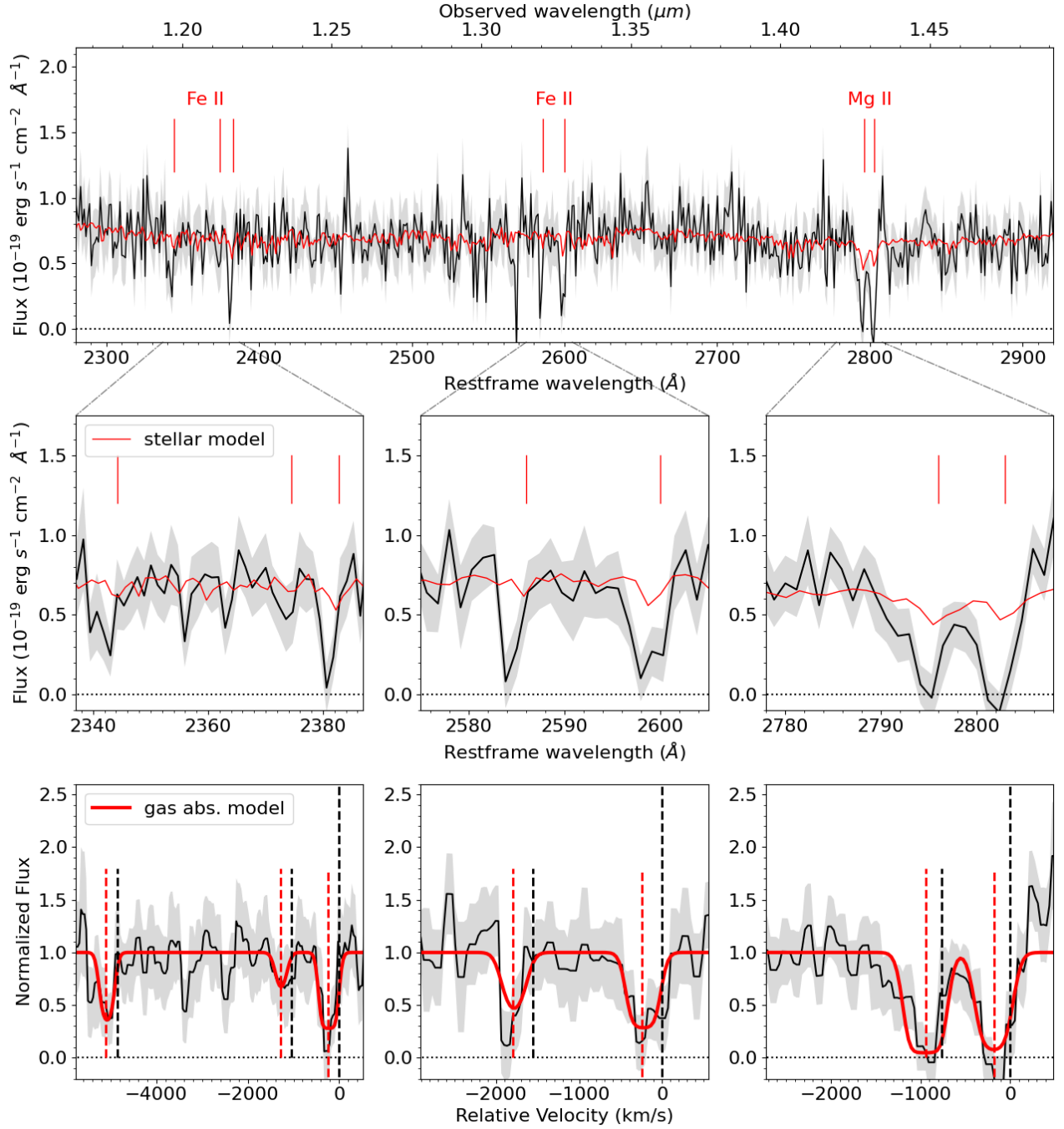


**Figure 3.** *Top:* The restframe UV spectrum (black) is shown with the model stellar continuum spectrum (red) derived from the best-fit parameters constrained by the restframe optical spectrum and normalized to the local continuum level. The spectrum features a series of Fe II and Mg II absorptions that are more pronounced than what would be expected from the stellar absorption alone. *Middle:* A zoomed-in view of the absorption lines. The red vertical lines mark the wavelengths of absorption at rest based on the redshift determined from the optical spectrum. The centers of the absorption lines are blueshifted. *Bottom:* The relative strength of the observed spectrum compared to the model stellar continuum. The thick red lines represent the best-fit ISM absorption models. Vertical dashed lines – both black and red – indicate the positions of absorption lines with zero velocity and the best-fit line centers, respectively. Both Fe II and Mg II are blueshifted by  $\sim 200 \text{ km s}^{-1}$  relative to the stellar continuum.

**Table 3.** Physical properties of Fe II and Mg II absorption lines and derived quantities

	Fe II	Mg II
$v / \text{km s}^{-1}$	$-236^{+25}_{-20}$	$-176^{+29}_{-28}$
$C_f$	$0.71^{+0.10}_{-0.11}$	$0.98^{+0.02}_{-0.09}$
$b / \text{km s}^{-1}$	$139^{+33}_{-26}$	$148^{+27}_{-40}$
	Fe II $\lambda 2374$	Mg II $\lambda 2803$
$\tau_0$	$0.75^{+0.76}_{-0.33}$	$4.7^{+7.8}_{-1.3}$
$W/\text{\AA}$	$0.81^{+0.25}_{-0.20}$	$3.80^{+0.53}_{-0.58}$
$\log(N(X)/\text{cm}^{-2})$	$14.89^{+0.15}_{-0.22}$	$14.27^{+0.07}_{-0.08}$
$\log[N(H)/\text{cm}^{-2}]$	$21.21^{+0.15}_{-0.22}$	$19.62^{+0.07}_{-0.08}$

blueshifted by  $\sim 200 \text{ km s}^{-1}$  relative to the stellar continuum. The high covering fractions are consistent with the visual inspection (Figure 3).

#### 4.2. Gas Column Density

In the optically thin case, the column density of the gas can be estimated with the linear relation of the curve of growth (e.g. Draine 2011)

$$N_{ion}[\text{cm}^{-2}] = 1.13 \times 10^{20} \frac{W_{ion}}{f\lambda^2} \frac{1}{C_f}, \quad (1)$$

where  $W_{ion}$  is the equivalent width of the absorption line in angstrom,  $f$  is the oscillator strength, and  $\lambda$  is the wavelength of the line.

The joint fit of the multiple Fe II indicates that only the weakest Fe II  $\lambda 2374$  line is optically thin ( $\tau_0 = 0.75$ , Table 3). The second weakest line, Fe II  $\lambda 2586$ , has an oscillator strength 2.2 times that of Fe II  $\lambda 2374$  thus  $\tau_0 > 1$ . Given this, I use the best-fit model of Fe II  $\lambda 2374$  (thick red line in the bottom panels in Figure 3) to estimate the gas column density. As for Mg II, even the weaker Mg II  $\lambda 2803$  line has  $\tau_0 \gg 1$ , therefore, only a lower limit of the column density can be obtained.

I integrated the best-fit models over the wavelength ranges of the lines to calculate the equivalent widths. In many runs of fitting, the models suggest that Mg II  $\lambda 2803$  is blended with Mg II  $\lambda 2796$ . In these cases, I take the wavelength with the highest flux between Mg II  $\lambda 2796$  and  $\lambda 2803$  as the bluest wavelength and integrate redwards to obtain the equivalent width of Mg II  $\lambda 2803$ . The equivalent widths of Fe II  $\lambda 2374$  and Mg II  $\lambda 2803$  and the derived Fe II and Mg II column densities are listed in Table 3.

Next, I use Fe II to estimate the total hydrogen column density. This calculation requires an understanding of the ionization state of iron, the metallicity of the gas, and the degree of dust depletion for the elements. Current available data do not contain all the information, I thus adopt commonly used values and note that

the derived hydrogen column densities depend on the assumptions.

Firstly, I assume that all Fe are singly ionized,  $\chi = n(\text{Fe II})/n(\text{Fe}) = 1$ . In Mg II absorbing clouds at  $z \sim 1$ , almost all Mg are singly ionized (Churchill et al. 2003). Given that the ionization potentials of neutral Mg and Fe (7.6 eV and 7.9 eV) and Mg II and Fe II (15.0 eV and 16.2 eV) are similar, it is reasonable to assume that Fe II is the dominant ion.

Secondly, elements in the gas phase can be significantly depleted onto dust grains, and the depleted fraction varies widely depending on the composition and of the grains and other properties of ISM (Savage & Sembach 1996). The depletion factor  $X$ , denoted as  $\delta(X)$ , is defined as the logarithmic difference between the gas-phase abundance and the cosmic abundance:  $\delta(X) = \log(X/H)_g - \log(X/H)_0$ . In the Galactic disk, the depletion factor for iron,  $\delta(\text{Fe})$ , ranges between -1.0 and -2.3 (Jenkins 2009). I adopt a median value of  $\delta(\text{Fe}) = -1.7$  based on the sample measured by Jenkins (2009). Additionally, I use the solar abundance  $\log(\text{Fe}/H) = -4.49$  (Savage & Sembach 1996) and assume the gas-phase metallicity is the same as the stellar metallicity (as listed in Table 2).

The hydrogen column density derived from Fe II absorption (Table 3) can thus be express as:

$$N(H) = 1.62 \times 10^{21} \text{ cm}^{-2} \left( \frac{1}{\chi(\text{Fe II})} \right) \left( \frac{N(\text{Fe II})}{10^{14.89} \text{ cm}^{-2}} \right) \left( \frac{10^{-4.49}}{10^{\log \text{Fe}/H}} \right) \left( \frac{Z/Z_\odot}{0.74} \right) \left( \frac{10^{-1.7}}{10^{\delta(\text{Fe})}} \right) \quad (2)$$

Table 3 also presents the lower limit of  $N_H$  derived from Mg II, assuming  $\chi = 1$ ,  $\log(\text{Mg}/H) = -4.42$ , and  $\delta(\text{Mg}) = -0.8$ , following the same references.

#### 4.3. Mass outflow rate

The  $\sim 200 \text{ km s}^{-1}$  blueshifted Fe II absorption and  $\sim 300 \text{ km s}^{-1}$  [O III] emission indicate the presence of outflowing gas in both neutral and ionized phases. To estimate the amount of outflowing gas in each phase, I make a few reasonable and common assumptions.

##### 4.3.1. Neutral outflow from [Fe II]

Under a simple assumption of thin-shell geometry of the outflowing gas, the mass and rate of the outflowing gas can be estimated as follows:

$$M_{out} = 1.4 m_p \Omega N_H R_{out}^2 \quad (3a)$$

$$\dot{M}_{out} = 1.4 m_p \Omega N_H R_{out} v_{out}, \quad (3b)$$

where  $m_p$  is the mass of the proton,  $\Omega$  is the solid angle subtended by the outflow,  $R_{out}$  is the radius of the



shell, and  $v_{out}$  is the velocity of the outflow (Rupke et al. 2005).

Neutral outflow are detected in  $\sim 45\%$  of massive ( $M_* > 10^{10} M_\odot$ ) galaxies at  $z \sim 2$  (Davies et al. 2024). Assuming that these galaxies have outflows with a similar geometry and are oriented randomly, this result implies that  $\Omega/4\pi > 0.45$ . I thus adopt  $\Omega = 0.45 \times 4\pi$ . Given that the covering fraction  $C_f$  of the outflow is close to 1 (Section 4.1), the physical extent of the outflowing gas should at least match the extent of the stellar light. Therefore, I conservatively assume  $R_{out} = 2R_e \simeq 800$  pc. It is worth noting that kilo-parsec scale neutral outflows have been reported for a quiescent galaxy at  $z \sim 3$  (D'Eugenio et al. 2023).

I then use the central velocity of the Fe II absorption lines as  $v_{out}$ , which provides a conservative estimate by assuming a narrow cone of outflow directed towards the observer. Consequently, the mass of the neutral outflow and the outflow rate estimated from the Fe II  $\lambda 2374$  line are as follows:

$$M_{out} = 6.3 \times 10^7 M_\odot \left( \frac{N_H}{1.63 \times 10^{21} \text{cm}^2} \right) \left( \frac{\Omega}{1.8\pi} \right) \left( \frac{R_{out}}{800 \text{pc}} \right)^2 \quad (4a)$$

$$\dot{M}_{out} = 20 M_\odot \text{yr}^{-1} \left( \frac{N_H}{1.63 \times 10^{21} \text{cm}^2} \right) \left( \frac{\Omega}{1.8\pi} \right) \left( \frac{R_{out}}{800 \text{pc}} \right) \left( \frac{v_{out}}{250 \text{ km s}^{-1}} \right) \quad (4b)$$

The outflow rate of  $20 M_\odot \text{yr}^{-1}$  is approximately 7 times higher than the SFR measured from the slit spectrum (Section 3.2). Even if the total SFR were twice higher (Section 2), the outflow rate would still exceed the SFR by more than 3 times.

#### 4.3.2. Ionized outflow from [O III]

The mass of ionized gas in the outflow can be estimated from the [O III] luminosity using the formula (Carniani et al. 2015):

$$M_{out,[OIII]} = \frac{1.4 m_p L_{[OIII]}}{n_e (n_O/n_H)_\odot (Z/Z_\odot) j}, \quad (5)$$

where  $m_p$  is the mass of the proton,  $n_e$  is the electron density, and  $j$  is the line emissivity. The term  $(n_O/n_H)_\odot (Z/Z_\odot)$  is the element abundance, with  $n_O/n_H = 10^{-3.13}$  (Savage & Sembach 1996) and  $Z/Z_\odot$  is taken from Table 2. Assuming a typical electron density of  $n_e \simeq 500 \text{ cm}^{-3}$  and a temperature of  $T_e \simeq$

$10^4 \text{ K}$  for the narrow-line region, the line emissivity is  $j = 3.4 \times 10^{-21} \text{ ergs s}^{-1} \text{ cm}^{-3}$  (Carniani et al. 2015). The mass outflow rate is then given by  $\dot{M}_{out,[OIII]} = M_{out,[OIII]} \times v/R_{out}$ . I adopt the central velocity of the [O III] emission  $v = 300 \text{ km s}^{-1}$  as the outflow velocity and an outflow radius  $R_{out} = 2R_e$ .

After correcting for the dust attenuation (Table 2), I derive the following values from the [O III] emission:  $L_{[OIII]} = 1.5 \times 10^{41} \text{ ergs s}^{-1}$ ,  $M_{ion,out} = 2.1 \times 10^5 M_\odot$  and  $\dot{M}_{ion,out} = 0.08 M_\odot \text{yr}^{-1}$ . The ionized outflow rate is orders of magnitude lower than the neutral outflow rate.

#### 4.3.3. Energy and momentum rates of outflow and AGN

I calculate the energy and momentum rate of the neutral outflow as  $E_{out} = \frac{1}{2} \dot{M}_{out} v_{out}^2 = 3.5 \times 10^{41} \text{ erg s}^{-1}$  and  $\dot{p}_{out} = \dot{M}_{out} v_{out} = 3.0 \times 10^{34} \text{ dyne}$ . The ionized outflow is not considered here due to its negligible contribution to the total energy and momentum rates.

I then assess whether the current AGN is energetic enough to drive the observed outflow. The bolometric luminosity of the AGN is estimated as  $L_{bol,AGN} = 600 L_{[OIII]}$ , with a systemic uncertainty of a factor of 2 (Netzer 2009). Numerical simulations suggest that only a small fraction, approximately  $\sim 5 - 15$  percent, of the bolometric luminosity is mechanically coupled to the ISM in order to produce realistic galaxies (Di Matteo et al. 2005; Booth & Schaye 2009; Kurosawa et al. 2009). For a conservative estimate, I adopt a lower value of 5% and calculate the energy and momentum fluxes from the AGN:  $\dot{E}_{AGN} = 0.05 \times L_{bol,AGN} = 6.0 \times 10^{42} \text{ erg s}^{-1}$  and  $\dot{p}_{AGN} = L_{AGN}/c = 4.0 \times 10^{35} \text{ dyne}$ . While this calculation is subject to systematic uncertainties, it demonstrates that AGN could indeed supply sufficient energy and momentum to drive the outflow.

## 5. DISCUSSION

Several massive quiescent galaxies at  $z > 4$  have been spectroscopically confirmed (Tanaka et al. 2019; Valentino et al. 2020; Carnall et al. 2023, 2024; Frye et al. 2024; Kakimoto et al. 2024; de Graaff et al. 2024). These objects challenge our understanding of quenching mechanisms, as they exhibit high SFRs in the past and significantly reduced SFRs in the present. For instance, at  $z \sim 4$ , the gas depletion timescale of a typical star-forming galaxy is  $\sim 500 \text{ Myr}$  (Dessauges-Zavadsky et al. 2020). This timescale is too long to explain the SFH of the quiescent galaxy discussed in this paper, which features an e-folding time of only 50 Myr.

At lower redshifts of  $z \simeq 2.5$  and  $z \simeq 3$ , compelling evidence for AGN-driven outflow as a quenching mechanism comes from two massive quiescent galaxies

(D’Eugenio et al. 2023; Belli et al. 2024). Both galaxies, observed with JWST, display line ratios of  $[\text{N II}]/\text{H}\alpha$  and  $[\text{O III}]/\text{H}\beta$  indicative of AGN activity, alongside blueshifted  $[\text{O III}]$  emission and Na I absorption. The estimated neutral outflow rates from Na I are more than 10 times the SFRs. This significant mass loading factor supports the interpretation of quenching driven by ejective SMBH feedback.

The quiescent AGN-host galaxy discussed in this paper presents a similar scenario at an even higher redshift. The neutral outflow rate is  $\sim 7$  times the SFR. This indicates that the gas reservoir is depleted mainly by the AGN-driven outflow rather than the star formation. Consequently, the SFR declines on a much shorter timescale than the typical gas depletion time observed in star-forming galaxies. Despite the weak line emission, the analysis in Section 4.3.3 demonstrates that the AGN is sufficiently powerful to supply the necessary energy and momentum to drive the outflow.

On the other hand, while ionized gas outflows are easier to detect, studies of AGN-host galaxies in the local universe reveal that the majority of gas ejection occurs in the neutral or molecular phase (Fiore et al. 2017; Baron et al. 2020; Avery et al. 2022). The ionized gas typically represents only a small fraction of the total mass ejected. Along with report at  $z = 2.5$  and  $z = 3$  (D’Eugenio et al. 2023; Belli et al. 2024), this galaxy shows a similar behavior at  $z = 4$ .

It is important to note that the measured outflow velocity of  $\sim 250 \text{ km s}^{-1}$  might not be sufficient to escape the gravitational potential of a massive galaxy halo. The gas could fall back and potentially fuel future star formation. Nevertheless, the case presented here underscores the capability of AGN-driven ejective feedback to trigger quenching, halt star formation at least temporarily, and help explain the presence of massive quiescent galaxies at  $z > 4$ .

## 6. SUMMARY AND CONCLUSION

This paper reports the first detection of neutral gas outflow from a massive quiescent galaxy at  $z > 4$ . Obtained by JWST NIRSpec, the restframe optical spectrum reveals high-ionization emission lines of  $[\text{Ne III}]$  and  $[\text{O III}]$ , while  $[\text{O II}]$  and  $\text{H}\beta$  are at most marginally detected. The emission line ratios indicate the presence of an AGN in this galaxy.

Modeling the stellar continuum absorption features yields a very low sSFR of  $5 \times 10^{-11} \text{ yr}^{-1}$ , roughly 40 times below than the star-forming main sequence at a similar redshift. Furthermore, the SFR of this galaxy has experienced a 40-fold decline over the last 400 Myr. Such a rapid truncation of star formation cannot be solely attributed to gas consumption.

In addition, the restframe UV spectrum shows blueshifted absorption features from Mg II and Fe II at  $\sim 250 \text{ km s}^{-1}$  relative to the stellar continuum, indicating outflowing neutral gas. The estimated outflow rate of neutral gas is around 7 times the current SFR. This suggests that the quenching of star formation is likely driven by AGN-induced outflows, offering an explanation to the presence of massive quiescent galaxies at  $z > 4$ .

- 1 I thank Prof. Lan Ting-Wen, Prof. Sirio Belli, Dr.
- 2 Adam Carnall, Prof. David Rupke, and Prof. Misawa
- 3 Toru for suggestions and fruitful discussion. I acknowl-
- 4 edge funding through the National Science and Technol-
- 5 ogy Council grant 111-2112-M-002-048-MY2 and 113-
- 6 2112-M-002-027-MY2. The data products presented
- 7 herein were retrieved from the Dawn JWST Archive
- 8 (DJA). DJA is an initiative of the Cosmic Dawn Cen-
- 9 ter (DAWN), which is funded by the Danish National
- 10 Research Foundation under grant DNR140.

*Software:* Astropy (Astropy Collaboration et al. 2013, 2018, 2022), BAGPIPES (Carnall et al. 2018), Galfit (Peng et al. 2010), pPXF (Cappellari & Emsellem 2004; Cappellari 2017), Matplotlib (Hunter 2007), Spectres (Carnall 2017)

## REFERENCES

- Abazajian, K. N., Adelman-McCarthy, J. K., Agüeros, M. A., et al. 2009, *ApJS*, 182, 543, doi: [10.1088/0067-0049/182/2/543](https://doi.org/10.1088/0067-0049/182/2/543)
- Astropy Collaboration, Robitaille, T. P., Tollerud, E. J., et al. 2013, *A&A*, 558, A33, doi: [10.1051/0004-6361/201322068](https://doi.org/10.1051/0004-6361/201322068)
- Astropy Collaboration, Price-Whelan, A. M., Sipőcz, B. M., et al. 2018, *AJ*, 156, 123, doi: [10.3847/1538-3881/aabc4f](https://doi.org/10.3847/1538-3881/aabc4f)
- Astropy Collaboration, Price-Whelan, A. M., Lim, P. L., et al. 2022, *ApJ*, 935, 167, doi: [10.3847/1538-4357/ac7c74](https://doi.org/10.3847/1538-4357/ac7c74)
- Avery, C. R., Wuyts, S., Förster Schreiber, N. M., et al. 2022, *MNRAS*, 511, 4223, doi: [10.1093/mnras/stac190](https://doi.org/10.1093/mnras/stac190)
- Backhaus, B. E., Trump, J. R., Cleri, N. J., et al. 2022, *ApJ*, 926, 161, doi: [10.3847/1538-4357/ac3919](https://doi.org/10.3847/1538-4357/ac3919)
- Backhaus, B. E., Trump, J. R., Pirzkal, N., et al. 2024, *ApJ*, 962, 195, doi: [10.3847/1538-4357/ad1520](https://doi.org/10.3847/1538-4357/ad1520)

- Baldry, I. K., Glazebrook, K., Brinkmann, J., et al. 2004, *ApJ*, 600, 681, doi: [10.1086/380092](https://doi.org/10.1086/380092)
- Baron, D., Netzer, H., Davies, R. I., & Xavier Prochaska, J. 2020, *MNRAS*, 494, 5396, doi: [10.1093/mnras/staa1018](https://doi.org/10.1093/mnras/staa1018)
- Bell, E. F., Wolf, C., Meisenheimer, K., et al. 2004, *ApJ*, 608, 752, doi: [10.1086/420778](https://doi.org/10.1086/420778)
- Belli, S., Park, M., Davies, R. L., et al. 2024, *Nature*, 630, 54, doi: [10.1038/s41586-024-07412-1](https://doi.org/10.1038/s41586-024-07412-1)
- Booth, C. M., & Schaye, J. 2009, *MNRAS*, 398, 53, doi: [10.1111/j.1365-2966.2009.15043.x](https://doi.org/10.1111/j.1365-2966.2009.15043.x)
- Bruzual, G., & Charlot, S. 2003, *MNRAS*, 344, 1000, doi: [10.1046/j.1365-8711.2003.06897.x](https://doi.org/10.1046/j.1365-8711.2003.06897.x)
- Calzetti, D., Armus, L., Bohlin, R. C., et al. 2000, *ApJ*, 533, 682, doi: [10.1086/308692](https://doi.org/10.1086/308692)
- Cappellari, M. 2017, *MNRAS*, 466, 798, doi: [10.1093/mnras/stw3020](https://doi.org/10.1093/mnras/stw3020)
- . 2023, *MNRAS*, 526, 3273, doi: [10.1093/mnras/stad2597](https://doi.org/10.1093/mnras/stad2597)
- Cappellari, M., & Emsellem, E. 2004, *PASP*, 116, 138, doi: [10.1086/381875](https://doi.org/10.1086/381875)
- Carnall, A. C. 2017, arXiv e-prints, arXiv:1705.05165, <https://arxiv.org/abs/1705.05165>
- Carnall, A. C., McLure, R. J., Dunlop, J. S., & Davé, R. 2018, *MNRAS*, 480, 4379, doi: [10.1093/mnras/sty2169](https://doi.org/10.1093/mnras/sty2169)
- Carnall, A. C., McLure, R. J., Dunlop, J. S., et al. 2023, *Nature*, 619, 716, doi: [10.1038/s41586-023-06158-6](https://doi.org/10.1038/s41586-023-06158-6)
- Carnall, A. C., Cullen, F., McLure, R. J., et al. 2024, arXiv e-prints, arXiv:2405.02242, doi: [10.48550/arXiv.2405.02242](https://doi.org/10.48550/arXiv.2405.02242)
- Carniani, S., Marconi, A., Maiolino, R., et al. 2015, *A&A*, 580, A102, doi: [10.1051/0004-6361/201526557](https://doi.org/10.1051/0004-6361/201526557)
- Chevallard, J., & Charlot, S. 2016, *MNRAS*, 462, 1415, doi: [10.1093/mnras/stw1756](https://doi.org/10.1093/mnras/stw1756)
- Churchill, C. W., Vogt, S. S., & Charlton, J. C. 2003, *AJ*, 125, 98, doi: [10.1086/345513](https://doi.org/10.1086/345513)
- Davies, R. L., Belli, S., Park, M., et al. 2024, *MNRAS*, 528, 4976, doi: [10.1093/mnras/stae327](https://doi.org/10.1093/mnras/stae327)
- de Graaff, A., Setton, D. J., Brammer, G., et al. 2024, arXiv e-prints, arXiv:2404.05683, doi: [10.48550/arXiv.2404.05683](https://doi.org/10.48550/arXiv.2404.05683)
- Dessauges-Zavadsky, M., Ginolfi, M., Pozzi, F., et al. 2020, *A&A*, 643, A5, doi: [10.1051/0004-6361/202038231](https://doi.org/10.1051/0004-6361/202038231)
- D'Eugenio, C., Daddi, E., Gobat, R., et al. 2021, *A&A*, 653, A32, doi: [10.1051/0004-6361/202040067](https://doi.org/10.1051/0004-6361/202040067)
- D'Eugenio, F., Perez-Gonzalez, P., Maiolino, R., et al. 2023, arXiv e-prints, arXiv:2308.06317, doi: [10.48550/arXiv.2308.06317](https://doi.org/10.48550/arXiv.2308.06317)
- Di Matteo, T., Springel, V., & Hernquist, L. 2005, *Nature*, 433, 604, doi: [10.1038/nature03335](https://doi.org/10.1038/nature03335)
- Draine, B. T. 2011, *ApJ*, 732, 100, doi: [10.1088/0004-637X/732/2/100](https://doi.org/10.1088/0004-637X/732/2/100)
- Falcón-Barroso, J., Sánchez-Blázquez, P., Vazdekis, A., et al. 2011, *A&A*, 532, A95, doi: [10.1051/0004-6361/201116842](https://doi.org/10.1051/0004-6361/201116842)
- Fiore, F., Feruglio, C., Shankar, F., et al. 2017, *A&A*, 601, A143, doi: [10.1051/0004-6361/201629478](https://doi.org/10.1051/0004-6361/201629478)
- Forrest, B., Annunziatella, M., Wilson, G., et al. 2020a, *ApJL*, 890, L1, doi: [10.3847/2041-8213/ab5b9f](https://doi.org/10.3847/2041-8213/ab5b9f)
- Forrest, B., Marsan, Z. C., Annunziatella, M., et al. 2020b, *ApJ*, 903, 47, doi: [10.3847/1538-4357/abb819](https://doi.org/10.3847/1538-4357/abb819)
- Forrest, B., Wilson, G., Muzzin, A., et al. 2022, *ApJ*, 938, 109, doi: [10.3847/1538-4357/ac8747](https://doi.org/10.3847/1538-4357/ac8747)
- Forrest, B., Cooper, M. C., Muzzin, A., et al. 2024, arXiv e-prints, arXiv:2404.19018, doi: [10.48550/arXiv.2404.19018](https://doi.org/10.48550/arXiv.2404.19018)
- Franzetti, P., Scodeggio, M., Garilli, B., et al. 2007, *A&A*, 465, 711, doi: [10.1051/0004-6361:20065942](https://doi.org/10.1051/0004-6361:20065942)
- Frye, B. L., Pascale, M., Pierel, J., et al. 2024, *ApJ*, 961, 171, doi: [10.3847/1538-4357/ad1034](https://doi.org/10.3847/1538-4357/ad1034)
- Hunter, J. D. 2007, *Computing in Science & Engineering*, 9, 90, doi: [10.1109/MCSE.2007.55](https://doi.org/10.1109/MCSE.2007.55)
- Ilbert, O., McCracken, H. J., Le Fèvre, O., et al. 2013, *A&A*, 556, A55, doi: [10.1051/0004-6361/201321100](https://doi.org/10.1051/0004-6361/201321100)
- Jenkins, E. B. 2009, *ApJ*, 700, 1299, doi: [10.1088/0004-637X/700/2/1299](https://doi.org/10.1088/0004-637X/700/2/1299)
- Kakimoto, T., Tanaka, M., Onodera, M., et al. 2024, *ApJ*, 963, 49, doi: [10.3847/1538-4357/ad1ff1](https://doi.org/10.3847/1538-4357/ad1ff1)
- Kurosawa, R., Proga, D., & Nagamine, K. 2009, *ApJ*, 707, 823, doi: [10.1088/0004-637X/707/1/823](https://doi.org/10.1088/0004-637X/707/1/823)
- Leja, J., Carnall, A. C., Johnson, B. D., Conroy, C., & Speagle, J. S. 2019, *ApJ*, 876, 3, doi: [10.3847/1538-4357/ab133c](https://doi.org/10.3847/1538-4357/ab133c)
- Madau, P., & Dickinson, M. 2014, *ARA&A*, 52, 415, doi: [10.1146/annurev-astro-081811-125615](https://doi.org/10.1146/annurev-astro-081811-125615)
- Maltby, D. T., Almaini, O., McLure, R. J., et al. 2019, *MNRAS*, 489, 1139, doi: [10.1093/mnras/stz2211](https://doi.org/10.1093/mnras/stz2211)
- Marsan, Z. C., Marchesini, D., Brammer, G. B., et al. 2015, *ApJ*, 801, 133, doi: [10.1088/0004-637X/801/2/133](https://doi.org/10.1088/0004-637X/801/2/133)
- Martin, C. L., & Bouché, N. 2009, *ApJ*, 703, 1394, doi: [10.1088/0004-637X/703/2/1394](https://doi.org/10.1088/0004-637X/703/2/1394)
- Maseda, M. V., van der Wel, A., Franx, M., et al. 2021, *ApJ*, 923, 18, doi: [10.3847/1538-4357/ac2bfe](https://doi.org/10.3847/1538-4357/ac2bfe)
- McConachie, I., Wilson, G., Forrest, B., et al. 2022, *ApJ*, 926, 37, doi: [10.3847/1538-4357/ac2b9f](https://doi.org/10.3847/1538-4357/ac2b9f)
- Morton, D. C. 2003, *ApJS*, 149, 205, doi: [10.1086/377639](https://doi.org/10.1086/377639)
- Muzzin, A., Marchesini, D., Stefanon, M., et al. 2013, *ApJ*, 777, 18, doi: [10.1088/0004-637X/777/1/18](https://doi.org/10.1088/0004-637X/777/1/18)
- Netzer, H. 2009, *MNRAS*, 399, 1907, doi: [10.1111/j.1365-2966.2009.15434.x](https://doi.org/10.1111/j.1365-2966.2009.15434.x)
- Peng, C. Y., Ho, L. C., Impey, C. D., & Rix, H.-W. 2010, *AJ*, 139, 2097, doi: [10.1088/0004-6256/139/6/2097](https://doi.org/10.1088/0004-6256/139/6/2097)

- Popesso, P., Concas, A., Cresci, G., et al. 2023, MNRAS, 519, 1526, doi: [10.1093/mnras/stac3214](https://doi.org/10.1093/mnras/stac3214)
- Rupke, D. S., Veilleux, S., & Sanders, D. B. 2005, ApJS, 160, 87, doi: [10.1086/432886](https://doi.org/10.1086/432886)
- Salim, S., Boquien, M., & Lee, J. C. 2018, ApJ, 859, 11, doi: [10.3847/1538-4357/aabf3c](https://doi.org/10.3847/1538-4357/aabf3c)
- Sanders, R. L., Shapley, A. E., Jones, T., et al. 2021, ApJ, 914, 19, doi: [10.3847/1538-4357/abf4c1](https://doi.org/10.3847/1538-4357/abf4c1)
- Savage, B. D., & Sembach, K. R. 1996, ApJ, 470, 893, doi: [10.1086/177919](https://doi.org/10.1086/177919)
- Schreiber, C., Glazebrook, K., Nanayakkara, T., et al. 2018, A&A, 618, A85, doi: [10.1051/0004-6361/201833070](https://doi.org/10.1051/0004-6361/201833070)
- Setton, D. J., Khullar, G., Miller, T. B., et al. 2024, arXiv e-prints, arXiv:2402.05664, doi: [10.48550/arXiv.2402.05664](https://doi.org/10.48550/arXiv.2402.05664)
- Simons, R. C., Papovich, C., Momcheva, I. G., et al. 2023, ApJS, 266, 13, doi: [10.3847/1538-4365/acc517](https://doi.org/10.3847/1538-4365/acc517)
- Straatman, C. M. S., Labbé, I., Spitler, L. R., et al. 2014, ApJL, 783, L14, doi: [10.1088/2041-8205/783/1/L14](https://doi.org/10.1088/2041-8205/783/1/L14)
- Strateva, I., Ivezić, Ž., Knapp, G. R., et al. 2001, AJ, 122, 1861, doi: [10.1086/323301](https://doi.org/10.1086/323301)
- Tanaka, M., Valentino, F., Toft, S., et al. 2019, ApJL, 885, L34, doi: [10.3847/2041-8213/ab4ff3](https://doi.org/10.3847/2041-8213/ab4ff3)
- Tanaka, M., Onodera, M., Shimakawa, R., et al. 2024, ApJ, 970, 59, doi: [10.3847/1538-4357/ad5316](https://doi.org/10.3847/1538-4357/ad5316)
- Tremonti, C. A., Moustakas, J., & Diamond-Stanic, A. M. 2007, ApJL, 663, L77, doi: [10.1086/520083](https://doi.org/10.1086/520083)
- Valentino, F., Tanaka, M., Davidzon, I., et al. 2020, ApJ, 889, 93, doi: [10.3847/1538-4357/ab64dc](https://doi.org/10.3847/1538-4357/ab64dc)
- Vazdekis, A., Koleva, M., Ricciardelli, E., Röck, B., & Falcón-Barroso, J. 2016, MNRAS, 463, 3409, doi: [10.1093/mnras/stw2231](https://doi.org/10.1093/mnras/stw2231)
- Ward, E., de la Vega, A., Mobasher, B., et al. 2024, ApJ, 962, 176, doi: [10.3847/1538-4357/ad20ed](https://doi.org/10.3847/1538-4357/ad20ed)
- Willmer, C. N. A., Faber, S. M., Koo, D. C., et al. 2006, ApJ, 647, 853, doi: [10.1086/505455](https://doi.org/10.1086/505455)